

# Plasticity of BCC micro-pillars controlled by competition between dislocation multiplication and depletion

*Ill Ryu <sup>\*a</sup>, William D. Nix <sup>a</sup>, Wei Cai <sup>b</sup>*

<sup>a</sup> *Department of Materials Science and Engineering,* <sup>b</sup> *Department of Mechanical Engineering, Stanford University, Stanford CA, 94305-4040, United States.*

\*Corresponding author

*E-mail address* : iryu@stanford.edu

*Present address*: 496 Lomita Mall, Durand Bldg., Rm. 129 Stanford University Stanford, CA 94305

*Tel/Fax*: +1 (650) 714-0731 / (650) 725 – 4034

---

## Abstract

Recent micro-pillar experiments have shown strong size effects at small pillar diameters. This ‘smaller is stronger’ phenomenon is widely believed to involve dislocation motion, which can be studied using dislocation dynamics (*DD*) simulations. In the present paper, we use a 3-D *DD* model to study the collective dislocation behavior in body-centered cubic (*BCC*) micro-pillars under compression. Following the molecular dynamics (*MD*) simulations of Weinberger and Cai, we consider a surface-controlled cross-slip process, involving image forces and non-planar core structures, that leads to multiplication without the presence of artificial dislocation sources or pinning points. The simulations exhibit size effects and effects of initial dislocation density and strain rate on strength, which appear to be in good agreement with recent experimental results and with a simple dislocation kinetics model described here. In addition, at the high strain rates considered, plasticity is governed mainly by the kinetics of dislocation motion, not their elastic interactions.

*Keywords*: plasticity, micro-pillars, dislocation dynamics, stress-strain relations

---

## 1. Introduction

As the technology of micro-scale devices evolves to smaller dimensions, plasticity at small scales attracts more and more attention. This is driven by the knowledge that many mechanical properties at the sub-micron scale differ from those at the continuum scale. From the recent micro-pillar compression experiments [1-3], it is now known that the flow stress of metallic micro-pillars increases with decreasing sample size even in the absence of significant hardening by geometrically necessary dislocations or strain gradients [4,5]. Recent review articles have summarized the current state of this research [6,7]. To understand the 'smaller is stronger' phenomenon in metals, several models have been proposed, most notably the dislocation starvation model [2,8,9] and the single arm source model [10-12]. In the dislocation starvation model, the small number of mobile dislocations present in sub-micron pillars is expected to annihilate at the nearby free surfaces during plastic flow, so that nucleation of new dislocations is required for further plastic deformation to occur. In general, higher stresses are required for dislocation nucleation than for activating existing dislocation sources. Since dislocations in smaller pillars might move out of the sample more quickly than they multiply, smaller samples are expected to have higher flow stresses. Recent *in-situ TEM* observations of *Ni* pillars under compression show that mechanical annealing can occur in sub-micron sized pillars [9]. In the single arm source model, the radius of the truncated *Frank-Read* source is smaller in smaller samples, so that the stress needed to activate the source is higher. As a result, smaller samples are predicted to have higher flow stresses. Support for the single arm source model can be found in the *in-situ TEM* observations [13,14].

Although *in-situ TEM* is a powerful tool for exploring the microscopic behavior of materials directly, it has several limitations. For example, it requires a very thin electron transparent section of material and the dislocations often move too fast to be observed clearly [15]. To contribute to a better understanding of small-scale plasticity, it helps to delve more deeply into the details of dislocation behavior, as dislocation motion is the primary mechanism for plastic deformation. In this sense, dislocation dynamics (*DD*) simulation provides a unique opportunity to explore the motion of individual dislocations, and allows us to develop a better microscopic understanding of the mechanical behavior of micro-pillars [16-18].

For metals with the face-centered cubic (*FCC*) crystal structure, *DD* simulations have provided significant insight into understanding the mechanical behavior at small scales in terms of the collective behavior of dislocations [12,19-24]. The same approach can be taken for *BCC* metals provided changes are made to account for the different dislocation mobilities and multiplication mechanisms. For *BCC* metals, dislocation plasticity is thought to be governed mainly by the motion of screw dislocations, which have a low mobility, attributed to a non-planar core structure and a high *Peierls* barrier [25-28]. In addition, from molecular dynamics (*MD*) simulations of plasticity of *BCC* nano-pillars, multiplication is expected to occur by a process of surface induced cross-slip, wherein isolated screw dislocations, aided by image stresses, can self-multiply and generate sources of dislocations [29,30].

In this paper, we implement an algorithm that accounts for surface cross-slip in *BCC* metal pillars under uniaxial loading in *DD* models and explore its effect on the macroscopic deformation behavior. Moreover, we compare our simulation results with recent experiments, which have shown that mechanical annealing and exhaustion hardening are also possible in *BCC* metals [31,32]. To better understand the results of these simulations, a simple dislocation kinetics model is developed, based on the competition between surface controlled multiplication and loss of dislocations by glide out of the micro-pillar. The *DD* simulation results and the kinetics model show similar effects of sample size and strain rate on the stress-strain curve.

## 2. Simulation methods

### 2.1. Three dimensional dislocation dynamics in a cylinder geometry

The dislocation dynamics simulations were performed using a modified version of *ParaDiS*, a *DD* code originally developed at the Lawrence Livermore National Laboratory [18]. In *ParaDiS*, dislocations are described as straight perfect dislocation segments connected by nodes. Based on the stress fields of the segments and the loading conditions, dislocation movements are computed and updated. In an effort to make the model conform to a micro-pillar compression experiment, the traction-free surface should be taken into

account. Modifications to the *ParaDiS* code have been made to account for the presence of the cylinder surface [33]. It considers dislocation motion only in the pre-defined cylinder region and deletes any dislocations outside of this cylinder region. A spectral method has been developed to compute the image stress field in order to satisfy the traction-free boundary condition on the cylinder surface. However, in this work, we include the effect of the image stress only for the surface nodes by specifying image stresses on them, because they play a critical role in the selection of slip planes and the activation of the surface cross-slip multiplication process. We have seen that ignoring the image stress for all other segments does not make a significant qualitative change in the simulations. Using the surface cross-slip algorithm, we performed *DD* simulations to explore the effects of sample size, initial dislocation density, and the strain rate on the stress-strain behavior under uniaxial loading.

## 2.2. Surface cross-slip mechanism

Recently, Weinberger and Cai [29], using *MD*, found that even a single, isolated screw dislocation in a *BCC* nano-pillar could multiply by a process involving cross-slip near the surface. They found that the image forces on a straight, inclined, screw dislocation act in opposite directions on either end of the dislocation, causing the two ends of the dislocation to move on different slip planes, the primary plane and the cross-slip plane. The pinning point so created serves as an anchoring point on the glide dislocation, which, above a critical stress, can spiral about that point and create multiple dislocations. Here, we develop a simple algorithm to implement surface-induced cross-slip in the *ParaDiS* cylinder code. For simplicity, we allow for slip to occur only on the  $1/2 \langle 111 \rangle / \{110\}$  type slip systems. Since only screw dislocations can cross-slip, here we consider a pure screw dislocation in the cylinder geometry, as shown in *Figure 1A*. The main task is to determine the slip planes of surface nodes. In *Figure 1B*, *Peach-Koehler* forces due to dislocation interaction and external loading are computed for each surface node. In addition, the image forces are specified at the surface nodes. The image forces act to move the surface nodes in opposite directions, as shown in *Figure 1C*. This may be understood by noting that dislocations tend to shorten their length to minimize their energy by rotating. By adding up these forces, the slip planes of the surface nodes are chosen so that the projected force is maximum on the chosen slip plane. In *Figure 1D*, the slip plane of the front

surface node (A) is the (101) plane, while the slip plane of the back node (B) is the  $(0\bar{1}1)$  plane. Initially, the dislocation is on a single slip plane, but it would move on two different slip planes due to the surface cross-slip mechanism. Because of the surface cross-slip, the dislocation would form a cusp with two arms on different slip planes and evolve into a spiral loop. Afterwards, because the edge dislocation segments move much faster than the screw segments, the loop expands mainly by edge motion. For the **DD** simulation, the mobility of the edge-character segments is set to be 100 times larger than that of the screw segments [29], and dislocation motion is limited to glide in specified slip planes, except for surface dislocation segments. Detailed information on the anisotropic mobility law is given in [34]. When the edge dislocation segments meet the surface, the one dislocation will have evolved into three dislocations. As a result, a single dislocation can self-multiply (see *supplementary movie 1A*). However, if the stress is lower than a critical stress for a given sized pillar, the cusp will move along the dislocation line and escape from the pillar so that surface multiplication will not occur (see *supplementary movie 1B*). Since the critical stress needed to cause the cusped dislocation to bow and multiply is controlled by an *Orowan* bowing-like process, the critical stress for multiplication is roughly inversely proportional to the diameter of the pillar.

### 2.3. Initial dislocation structure

Since the initial dislocation configuration affects the stability of pinning points, it is expected to have a significant effect on the mechanical response of the micro-pillars [23]. For the modeling of **FCC** metals, several initial configurations have been suggested: a *Frank* network relaxed from randomly distributed straight and jogged dislocations [20], randomly distributed *Frank-Read* sources with pinning points [24] and randomly distributed loops with cross-slip allowed [23]. However, these structures are not especially relevant to **BCC** metals because of the different edge/screw dislocation mobilities. Moreover, the physical origin of potentially permanent pinning points has remained unknown in sub-micron pillars, based on **MD** simulations [35].

In the **MD** study of **BCC** nano-pillars by Weinberger and Cai [29], if a single dislocation is placed in a cylinder, it tends to rotate into a screw orientation to reduce its energy. Because only a few dislocations

would exist in sub-micron sized pillars, dislocations would rarely interact with others without external loading. Moreover, since the mobility of the screw orientation is much lower than that of edge, plasticity in **BCC** micro-pillars is expected to be governed by screw dislocation motion. As a result, our **DD** simulation starts with a configuration of randomly distributed pure screw dislocations prior to loading.

### 3. Simulation Results

#### 3.1. Size-dependence of flow stress

To investigate the effect of sample size, simulations were performed with different pillar diameters ranging from 150 nm to 1  $\mu\text{m}$  under periodic boundary conditions along the cylinder axis. For these simulations, a constant axial strain rate of  $10^5 \text{ s}^{-1}$  was imposed. This is very much higher than typical experimental strain rates of  $10^{-3} \text{ s}^{-1}$  or  $10^{-4} \text{ s}^{-1}$ . Due to timescale limitations, we have not yet been able to model experimental strain rates. The initial dislocation density was  $10^{13} \text{ m}^{-2}$ , which amounts to just a few dislocations in the smallest pillars and a much higher line content in the largest pillars. With these conditions, the **DD** simulation predicts that the stress-strain curve clearly depends on pillar diameter, as shown in **Figure 2**. As the sample size decreases from 1  $\mu\text{m}$  to 150 nm in diameter, the flow stress increases from roughly 600MPa to 1.6GPa. In addition, smaller samples show 'jerky' flow behavior while the stress-strain curves for larger samples are relatively smooth, consistent with experiment [31,32]. The evolving dislocation densities for differently sized pillars have also been calculated and are plotted against strain in **Figure 3A-3D**. Interestingly, the dislocation density for the largest diameter sample (1  $\mu\text{m}$ ) increases continuously, while the dislocation density for the smallest sample (150 nm diameter) shows significant fluctuation but overall remains roughly constant with increasing plastic deformation. *Supplementary movies 2A and 2B* show the evolution of the dislocation structure, the corresponding stress-strain curves and the evolving dislocation density for both the smallest (150 nm) and the largest (1  $\mu\text{m}$ ) diameters, respectively. The colors of the segments indicate the *Burgers* vectors of the various dislocations, among which the red segments indicate newly created dislocation junctions, formed through reactions of the type  $a/2[1\bar{1}1] + a/2[11\bar{1}] = a[100]$ , while the green segments

indicate glide dislocations with *Burgers* vectors of the type  $a/2 \langle 111 \rangle$ . As shown in *supplementary movie 2A*, dislocations in the smallest pillar escape the pillar so easily that the dislocation density never rises to a high value, with the consequence that few dislocation junctions are formed. On the other hand, as shown in *supplementary movie 2B*, dislocation multiplication is prolific in the largest pillar, spreading dislocations over the entire volume of the cylinder and causing a high density of junctions to form.

To see the size dependence clearly, the flow stresses for a plastic strain of 0.6% were determined and plotted against the corresponding pillar diameters in *Figure 4*. To make this plot, we take the flow stresses over 7 or 9 simulations with random initial conditions for a given sized pillar. The log-log plot gives a size dependence exponent of about -0.48, which is roughly consistent with experimental exponents for *BCC* metals: -0.24 to -0.48 [28,30,36,37].

### 3.2. *Effect of initial dislocation density*

To study the effect of the initial dislocation density, we have performed simulations with different initial densities ranging from  $10^{13} m^{-2}$  to  $8 \times 10^{13} m^{-2}$ . For these simulations, a constant strain rate of  $10^5 s^{-1}$  was imposed and the pillar diameter was 150 nm. Stress-strain curves for three different initial dislocation densities are shown in *Figure 5*. We see that the flow stress decreases with increasing initial dislocation density, which is not consistent with the Taylor hardening relationship. However, it can be understood by the fact that the higher dislocation density would result in a softer response by increasing the plastic strain rate, through the *Orowan* formula, and consequentially decreasing the flow stress rate. These results suggest that *Taylor* hardening effects are smaller than the softening effects of dislocations as carriers of plasticity.

These results are in good agreement with the micro-compression experiments of Bei *et al.* on *Mo* pillars [38], wherein pre-straining results in a softer response. Because more highly pre-strained pillars would be expected to have a higher initial dislocation density, the inverse proportionality between initial density and the flow stress predicted by the *DD* simulation is in accord with experimental results.

### 3.3. *Effect of strain rate*

We have also performed simulations for different high strain rates, ranging from  $10^5 \text{ s}^{-1}$  to  $10^6 \text{ s}^{-1}$ . Here, the initial dislocation density is again taken to be  $10^{13} \text{ m}^{-2}$  and the pillar diameter is  $150 \text{ nm}$ . The stress-strain curves for different strain rates are plotted in **Figure 6**. At the initial stage of loading, the pillar subjected to a higher strain rate starts to deform plastically at a higher stress (strain), so that the yield stress increases with increasing strain rate. However, the steady state flow stresses all converged to about  $1.6 \text{ GPa}$  after around 1.5% strain. As a result, the **DD** model shows a rate-insensitive steady-state flow stress. However, it must be repeated that the strain rates for the simulations are much higher than those used in experiments, so that a direct comparison with experiments is not yet possible.

#### **4. Dislocation kinetics model for micro-pillar plasticity controlled by self-multiplication**

In an effort to better understand plasticity controlled by the surface cross-slip mechanism, we have developed a simple dislocation kinetics model similar to the one suggested by Nix and Lee [39] for the case of surface nucleation controlled plasticity. A basic assumption of this model is that a fraction of dislocations will self-multiply after it has traveled a distance  $\ell$ , which is approximated by the diameter of a curved dislocation segment under the given stress.

The dislocation density is naturally controlled by the competition between the multiplication rate from the surface cross-slip mechanism and the depletion rate associated with dislocations moving out of the surface. Thus the density evolution can be expressed by

$$\dot{\rho} = \dot{\rho}_+ + \dot{\rho}_-, \quad (1)$$

where  $\dot{\rho}_+$  stands for the multiplication rate and  $\dot{\rho}_-$  is the depletion rate. Adapting the expression for  $\dot{\rho}_-$  given by Nix and Lee [39],  $\dot{\rho}_-$  may be approximated by the current dislocation density divided by the lifetime of the

dislocation,  $t_{life} = D/\bar{v}$ , where  $D$  is the diameter of the sample and  $\bar{v}$  is the average velocity of dislocations.

Using a linear mobility law, the dislocation depletion rate is

$$\dot{\rho}_- = -\beta \frac{\rho}{t_{life}} = -\beta \rho \frac{M \tau b}{D} = -\beta' \rho \frac{M \sigma b}{D}, \quad (2)$$

where  $\rho$  is the current dislocation density,  $\sigma$  is the stress along the loading axis and  $\beta$  and  $\beta'$  are constants.

For the multiplication rate, we take the frequency of the dislocation multiplication to be approximated by the average velocity of the screw dislocation divided by the size of the dislocation loop that can be supported by the given stress. Using the expression for the critical bowing stress for a *Frank-Read* source, the size of the loop can be approximated by

$$\ell = \frac{\mu b}{\tau}, \quad (3)$$

where  $\tau$  is the resolved shear stress. For simplicity, we omit the logarithmic term usually included in this relation. Together with a linear mobility law, the multiplication rate can then be expressed by

$$\dot{\rho}_+ = \alpha \rho \frac{\bar{v}}{\ell} = \frac{\alpha \rho M \tau^2}{\mu} = \frac{\alpha' \rho M \sigma^2}{E}, \quad (4)$$

where  $E$  is the elastic modulus and  $\alpha$ ,  $\alpha'$  are constants which describe the fraction of dislocations which will self-multiply. Then the dislocation density evolution law is

$$\dot{\rho} = \dot{\rho}_+ + \dot{\rho}_- = \rho M \left( \alpha' \frac{\sigma^2}{E} - \beta' \frac{\sigma b}{D} \right) \quad (5)$$

To compare the dislocation kinetics model with our **DD** simulations, a constant strain rate needs to be imposed. Thus, the axial stress can be computed as follows:

$$\dot{\sigma} = E \left( \dot{\varepsilon}^{total} - \dot{\varepsilon}^{pl} \right) = E \left( \dot{\varepsilon}^{applied} - \dot{\varepsilon}^{pl} \right), \quad (6)$$

Using *Orowan's* formula for the plastic strain rate and a linear mobility law, the resolved shear stress is then

$$\tau = \frac{\dot{\varepsilon}^{pl}}{\rho b^2 M}, \quad (7)$$

where  $\dot{\varepsilon}^{pl}$  is the shear strain rate. Considering the *Taylor* hardening effect, we modified the expression for the resolved flow stress as follows:

$$\tau = \frac{\dot{\varepsilon}^{pl}}{\rho b^2 M} + \gamma \mu b \sqrt{\rho}, \quad (8)$$

where  $\gamma$  is the Taylor hardening coefficient. Finally, the rate of change of the stress is then

$$\dot{\sigma} = E \left( \dot{\varepsilon}^{applied} - S \dot{\varepsilon}^{pl} \right) = E \left[ \dot{\varepsilon}^{applied} - S \rho b^2 M \left( \sigma S - \gamma \mu b \sqrt{\rho} \right) \right], \quad (9)$$

where  $S$  is the *Schmid* factor in the typical BCC slip system.

To assess the validity of the dislocation kinetics model, the dislocation density (*equation 5*) and the stress (*equation 9*) were numerically solved and plotted in *Figure 7, 8*. For comparison, *DD* simulation results were also plotted as shaded bands. For the plot,  $\alpha'$ ,  $\beta'$  and  $\gamma$  are chosen to be 0.096, 0.264 and 0.3 respectively, and  $M$  is set to be four times higher than the pure screw mobility in the *DD* model. In *Figure 7*, in order to check if the size effect could be predicted by the kinetics model, the diameter varies from 150 nm to 1  $\mu$ m with a constant strain rate of  $10^5 s^{-1}$  and an initial dislocation density of  $10^{13} m^{-2}$ , which are the same conditions used for the *DD* simulations. The kinetics model clearly shows the size effect on the flow stress: as the sample size decreases, the flow stress increases. Moreover, flow stresses and dislocation densities of various sized pillars are within the range of the *DD* simulation results, as shown in *Figures 3 and 7*.

According to the kinetics model, *without Taylor* hardening both the flow stress and the dislocation density eventually reach steady state values. By setting  $\dot{\rho}$ ,  $\dot{\sigma}$  and  $\gamma$  equal to zero, steady state values of  $\rho_{ss}$  and  $\sigma_{ss}$  are found as follows.

$$\sigma_{ss} = \frac{\beta' E b}{\alpha' D} \quad (10)$$

$$\rho_{ss} = \frac{\alpha' \dot{\epsilon}^{applied} D}{\beta' S^2 b^3 M E} \quad (11)$$

These steady state values for the stress are plotted for each pillar diameter as horizontal dashed lines in **Figures 7 and 8**. The stress-strain curves from the kinetics model *with Taylor* hardening converge to these steady state values asymptotically, except for the largest pillar, where *Taylor* hardening becomes significant. The contribution of *Taylor* hardening for the largest pillar is to be expected from the sharp increase in the dislocation density for that pillar, as shown in **Figure 3D**.

In addition to the size effect, the kinetics model clearly shows a rate insensitivity of the steady state flow stress, similar to the **DD** simulations, as shown in **Figure 8A**. That is to say, the steady state flow stress, as predicted by the **DD** simulations, is independent of the strain rate. As a consequence, the dislocation density remains roughly constant within the range of the **DD** simulations during further deformation, as shown in **Figure 8B**.

## 5. Discussion

In bulk **FCC** metals, plastic flow is strongly influenced by junction formation through the elastic interactions of dislocations. The critical stress to bow dislocations between obstacles often plays a dominant role in plastic flow and hardening. Dislocations are assumed to glide quickly from one obstacle to the next so that the kinetics of dislocation motion plays a relatively minor role. By contrast, for the **BCC** micro-pillars studied here, the results of the **DD** simulations as well as the predictions of the kinetics model suggest that at the high strain rates being considered, the size effect on the flow stress arises mainly from dislocation mobility and mobile dislocation density effects. This is also indicated by the simulations which show the yield stress decreases with increasing initial dislocation density. This is broadly consistent with the findings of Bei *et al.*[38] who showed that pre-straining of **Mo** alloy pillars leads to softening. Consistent with this picture, both the **DD** simulations and the kinetics model show a strain softening effect associated with the

multiplication of dislocations. This is reminiscent of the kind of plastic flow studied by Johnston and Gilman [40]. Thus, neither the dislocation starvation/nucleation model nor the single arm source model provides a good account of the size dependence of the strength of *BCC* micro-pillars at the high strain rates under this study.

The conclusion that the single arm source model does not describe the simulated flow behavior well might seem to be at odds with some of the features included in the modeling. In both the *DD* simulations and the kinetics modeling, *Orowan* bowing effects, with lengths that scale with the size of the pillars, play a key role. In particular, a critical stress for multiplication, which depends inversely on the pillar diameter, is a central feature of this modeling. This might seem to be identical to the single arm source model wherein the strength of the micro-pillar is directly related to the critical stress needed to bow a dislocation segment with a length that scales with the pillar diameter. But, in the present modeling critical stress does not determine the flow stress directly. Rather, it controls the flow stress indirectly through the multiplication of dislocations. In spite of this indirect relation, the steady state flow stress predicted by the kinetics model (equation 10 - without strain hardening) still takes a form that is reminiscent of the predictions of the single arm source model. The finding that the yield stress of the simulated micro-pillars increases dramatically with decreasing initial dislocation density (*Figure 5*), is the best way to see this distinction. If the single arm source model were controlling the strength directly, the yield strength would not be expected to increase so dramatically with decreasing initial dislocation density.(repeat)

As shown in Figure 8A, both the *DD* model and the kinetics model predict a strong strain rate sensitivity of the yield stress. This is broadly consistent with experiment, as recent micro-compression experiments on sub-micron Mo pillars [27] have shown the flow stress to be strain rate sensitive. However, the rate sensitivity of the yield stress in the present modeling is greater than that observed in the experiments. This is caused by the very high strain rates in the present simulations and the associated linear mobility law we have used. At larger plastic strains the predicted flow stresses for different strain rates tend to converge and lead to a smaller strain rate sensitivity. Eventually, at least for the case of no Taylor hardening, steady state flow conditions are predicted, wherein the steady state flow stress is completely independent of strain

rate. This is caused by the fact that the steady state flow stress is completely determined by the competition between a stress-dependent multiplication rate and a stress-independent loss rate. Thus the steady state flow stress and associated velocity becomes independent of the strain rate, making the dislocation density directly proportional to the strain rate through the *Orowan* relation. In the presence of *Taylor* hardening such steady states are not predicted. Finally, we note that the compression experiments on sub-micron Mo pillars [27] were conducted under load-controlled conditions. Under these conditions, the strain softening effects shown in the modeling and which eventually lead to steady states could not have been observed. Once strain softening begins, a plateau in the load-controlled stress-strain curve would be observed. The flow stresses reported in [27] should then correspond to the peak stresses in the simulated stress-strain curves, which do show a strong strain rate sensitivity.

Most existing *DD* simulations use a simple linear mobility law, in which the velocity of the dislocation segment is proportional to the resolved stress. However, in *BCC* metals, it is known that the velocity of a screw dislocation is not linearly proportional to the resolved stress due to lattice resistance [41]. Since screw dislocation motion could play an important role in plasticity of *BCC* metals, it would be useful to modify the mobility law using empirical forms [42,43]. With a nonlinear mobility law, a smaller size dependence exponent might be expected for lower, more realistic, strain rates, based on the findings of Lee and Nix [44]. They showed that smaller exponents are expected when the size-independent friction stress is large compared to the flow stress. Further work is needed to account for nonlinear mobility behavior, especially at low stresses in *BCC* metals.

In the *DD* simulations, dislocation multiplication occurs intermittently so that the dislocation density shows high fluctuations. This stochastic flow behavior is especially pronounced in the smallest pillars. Since the kinetics model is based on the collective behavior of dislocations, this kind of 'jerky' flow behavior cannot be predicted, so that the dislocation density in the kinetics model evolves smoothly, as shown in *Figures 7 and 8*. In the *DD* simulations, the frequency of the fluctuation in the dislocation density is very high, especially for the smallest pillars. Because there is no direct link between the dislocation density and the flow stress, as in the simple kinetics model, the flow stress in the *DD* simulations is not as sensitive to those abrupt

changes in dislocation density. As a consequence, the predicted flow stress in the kinetics model, where there is a direct link between the flow stress and the dislocation density, shows much higher oscillations than those found in the *DD* simulations, as seen in *Figures 7 and 8*. As we have pointed out several times, the present modeling of plasticity of *BCC* micro-pillars is limited in the sense that it applies to very high strain rates, much higher than those used in experiments. Further work is needed to extend this analysis to experimental strain rates.

## 6. Conclusions

In this research, 3D *DD* simulations have been performed in order to investigate the effects of sample size, initial dislocation density and strain rate on the stress-strain relations of *BCC* sub-micron metal pillars under uniaxial loading. The *DD* simulations including a surface cross-slip multiplication mechanism show that the flow stress increases with decreasing pillar size, decreasing initial dislocation density. They also show that yield stress is strongly strain rate sensitive.. These findings leads us to the notion that at the high strain rates considered, plasticity is mainly governed mainly by dislocation mobility and mobile dislocation density effects, not their elastic interactions. We also develop a dislocation kinetics model, based on the competition between multiplication due to the surface cross-slip mechanism and depletion by glide out of the micro-pillar. Results from both the *DD* model and kinetics model are in good agreement with recent experiments in *BCC* metal pillars.

## Acknowledgements

Support of this work by the Office of Science, Office of Basic Energy Sciences, of the U.S. Department of Energy under Contract No. DE-FG02-04ER46163 is gratefully acknowledged. This work is partially supported by the NSF Career Grant CMS-0547681. We would like to thank Dr. S.W. Lee of California Institute of Technology for useful discussions.

## References

- [1] Uchic MD, Dimiduk DM, Florando JN, Nix WD, Science 2004; 305:986.
- [2] Greer JR, Oliver WC, Nix WD. Acta Mater 2005;53:1821.
- [3] Volkert CA, Lilleodden ET. Philos Mag 2006;86:5567.
- [4] Fleck NA, Muller GM, Ashby MF, Hutchinson JW. Acta Metall Mater 1994;42:475.
- [5] Nix WD, Gao H., J Mech Phys Solids 1998;46:411.
- [6] Kraft O, Gruber P, Monig R, Weygand D, Annual Rev Mater Res 2010; 40:293.
- [7] Greer JR, De Hosson JTM, Prog Mater Sci 2011; 56:654.
- [8] Greer JR, Nix WD, Phys Rev B 2006; 73:245410.
- [9] Shan ZW, Mishra RK, Asif SAS, Warren OL, Minor AM, Nat Mater 2008; 7:115.
- [10] Parthasarathy TA, Rao SI, Dimiduk DM, Uchic MD, Trinkle DR, Scr Mater 2007; 56: 313.
- [11] Rao SI, Dimiduk DM, Parthasarathy TA, Uchic MD, Tang M, Woodward C, Acta Mater 2008;56: 3245.
- [12] Rao SI, Dimiduk DM, Tang M, Parthasarathy TA, Uchic MD, Woodward C, Phil Mag 2007;87: 4777.
- [13] Oh SH, Legros M, Kiener D, Dehm G, Nat Mater 2009; 8:95.
- [14] Kiener D, Minor AM, Nano Lett 2011;11:3816.
- [15] Williams DB; Carter CB, Transmission Electron Microscopy: a Textbook for Materials Science, first ed. New York: Plenum Press;1996.

- [16] Devincere B, Kubin LP, Mater Sci Eng A 1997; 234–236:8.
- [17] Schwarz KW, J Appl Phys 1999;85:120.
- [18] Arsenlis A, Cai W, Tang M, Rhee M, Opperstrup T, Hommes G, Pierce TG, Bulatov VV, Model Simul Mater Sci Eng 2007;15:553.
- [19] Espinosa HD, Panico M, Berbenni S, Schwarz KW. Int J Plasticity 2006;22:2091.
- [20] Tang H, Schwarz KW, Espinosa HD Phys Rev Lett 2008;100:185503.
- [21] El-Awady JA, Wen M, Ghoniem NM, J Mech Phys Solids 2009;57:32.
- [22] Liu ZL, Liu XM, Zhuang Z, You XC, Scr Mater 2009;60: 594.
- [23] Motz C, Weygand D, Senger J, Gumbsch P, Acta Mater 2009;57:1744.
- [24] Senger J, Weygand D, Motz C, Gumbsch P, Kraft O, Phil Mag 2010;90:617.
- [25] Cai W, Bulatov VV, Mater Sci Eng A 2004;277:387.
- [26] Brinckmann S, Kim JY, Greer JR, Phys Rev Lett 2008;100:155502.
- [27] Schneider AS, Clark BG, Frick CP, Gruber PA, Arzt E, Mater Sci Eng A 2009;508:241.
- [28] Schneider AS, Kaufmann D, Clark BG, Frick CP, Gruber PA, Monig R, Kraft O, Arzt E, Phys Rev Lett 2009;103:105501.
- [29] Weinberger CR, Cai W, Proc Natl Acad Sci 2008;105:14304.
- [30] Greer JR, Weinberger CR, Cai W, Mater Sci Eng A 2008;493:21.
- [31] Chisholm C, Bei H, Lowry M, Oh J, Syed Asif SA, Warren OL, Shan ZW, George EP, Minor AM, in press, 2012.

- [32] Huang L, Li QJ, Shan ZW, Li J, Sun J, Ma E, Nature comm 2011;2:547.
- [33] Weinberger CR, Cai W, J Mech Phys Solids 2007;55: 2027.
- [34] Cai W, Bulatov VV, Mater. Sci. Eng., A 2004; 387:277.
- [35] Weinberger CR, Cai W, Scripta Mater 2011;64:529.
- [36] Kim JY, Greer JR, Acta Mater 2009;57:5245.
- [37] Kim JY, Jang D, Greer JR, Acta Mater 2010;58:2355.
- [38] Bei H, Shim S, Pharr GM, George EP, Acta Mater 2008;56:4762.
- [39] Nix WD Lee SW, Phil Mag 2010; 91:1084.
- [40] Johnston WG , Gilman JJ, J Appl Phys 1959;30:129.
- [41] Gilbert MP, Queyreau S, Marian J, Phys. Rev. B 2011;84:174103
- [42] Gilman JJ, Aust J Phys 1960;13:327.
- [43] Prekel HL, Lawley A, Conrad H, ACTA METALL MATER 1968 ;16:337
- [44] Lee SW, Nix WD, Phil Mag 2011; 92:1238.

## Figure captions

Figure 1. (a) single screw dislocation and its slip planes in a cylinder and (b) *Peach-Koehler* forces (c) image forces and (d) total forces on front and back nodes.

Figure 2. Stress vs. strain curves for the 150 nm, 250 nm, 350 nm and 1  $\mu\text{m}$  sized pillars with random initial configurations.

Figure 3. Dislocation density evolution for the (a) 150 nm, (b) 250 nm, (c) 350 nm and (d) 1  $\mu\text{m}$  sized pillars from *DD* simulation(solid lines) and kinetics model(dashed lines).

Figure 4. Stress at 0.6% plastic strain as a function of pillar diameter. Table shows the average stress among 7~9 *DD* models with corresponding sized pillars.

Figure 5. Stress vs. strain curves with various initial dislocation densities ( $10^{13}$ ,  $4 \times 10^{13}$ , and  $8 \times 10^{13}$  [ $\text{m}^{-2}$ ]).

Figure 6. Stress vs. strain curves with various strain rate ( $1 \times 10^5$ ,  $5 \times 10^5$ , and  $1 \times 10^6$  [ $\text{sec}^{-1}$ ]).

Figure 7. Numerically solved stress vs. strain curves from the kinetics model with various sized pillars (150 nm, 250 nm, 350 nm, 500nm, and 1  $\mu\text{m}$ ) (solid lines). The steady state values without hardening effect are plotted in dashed lines. Banded plot corresponds to the *DD* simulation results for different sized pillars.

Figure 8. (a) Numerically solved stress vs. strain curves (solid line) from the kinetics model with various strain rate ( $1 \times 10^5$ ,  $5 \times 10^5$ , and  $1 \times 10^6$  [ $\text{sec}^{-1}$ ]). The steady state value without hardening effect is plotted in dashed lines. Banded plot corresponds to the *DD* simulation results for different sized pillars. (b) Dislocation density vs. strain curves (solid lines). *DD*

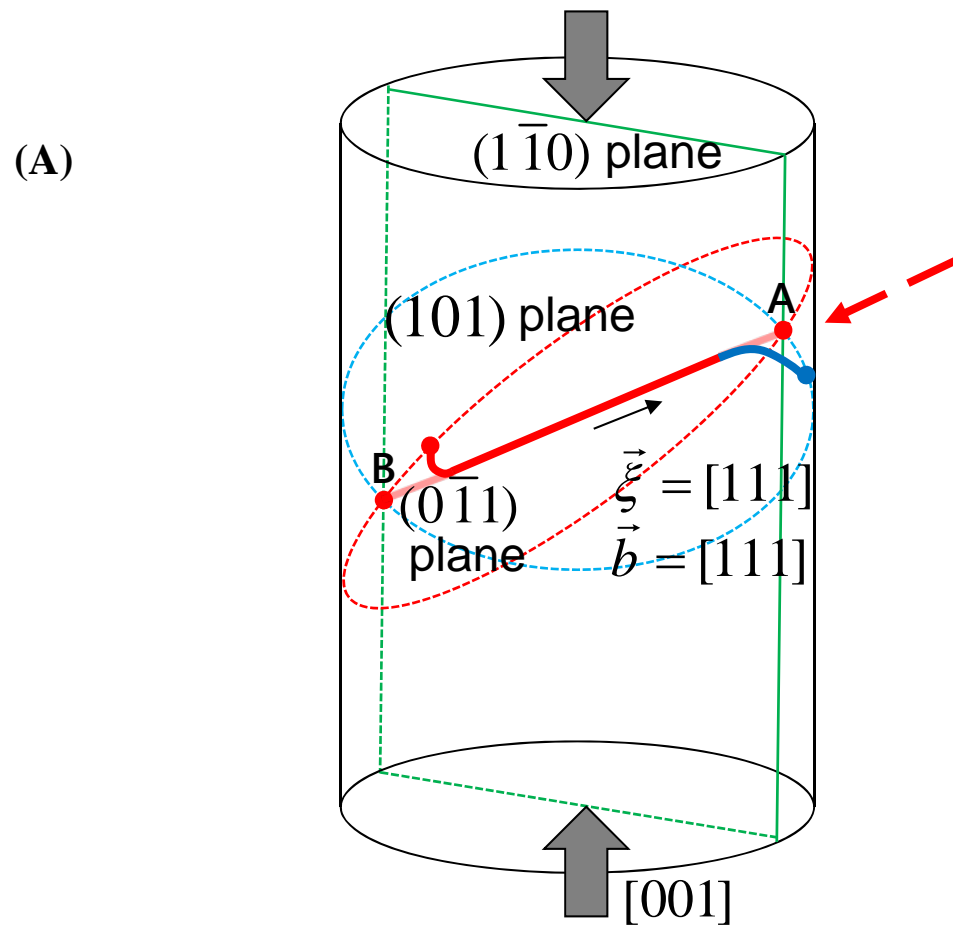
simulation results also plotted in red ( $1 \times 10^5$  [sec<sup>-1</sup>]), blue ( $5 \times 10^5$  [sec<sup>-1</sup>]), and black ( $10^6$  [sec<sup>-1</sup>]) lines.

### Supporting movie 1

**DD** simulation on a screw dislocation in a cylinder (a) above the critical stress, and (b) below the critical stress. The diameter of the cylinder is 150 nm, and strain rate is  $10^5$  [sec<sup>-1</sup>]. Above the critical stress, a single screw dislocation can multiply due to the surface cross slip. On the other hand, below the critical stress, the dislocation moves out of the cylinder after the cusp moves along the dislocation line. Dislocation segments are colored according to their slip planes.

### Supporting movie 2

**DD** simulation results for (a) 150 nm, (b) 1  $\mu$ m sized pillars under compression. The initial dislocation density is  $10^{13}$  [m<sup>-2</sup>] and strain rate is  $10^5$  [sec<sup>-1</sup>]. Upper movies show the dislocation structure evolution when viewed along the pillar axis (left) and from the side (right). Lower left shows stress strain curve and lower right shows dislocation density evolution. Dislocation segments are colored according to their Burgers vectors.



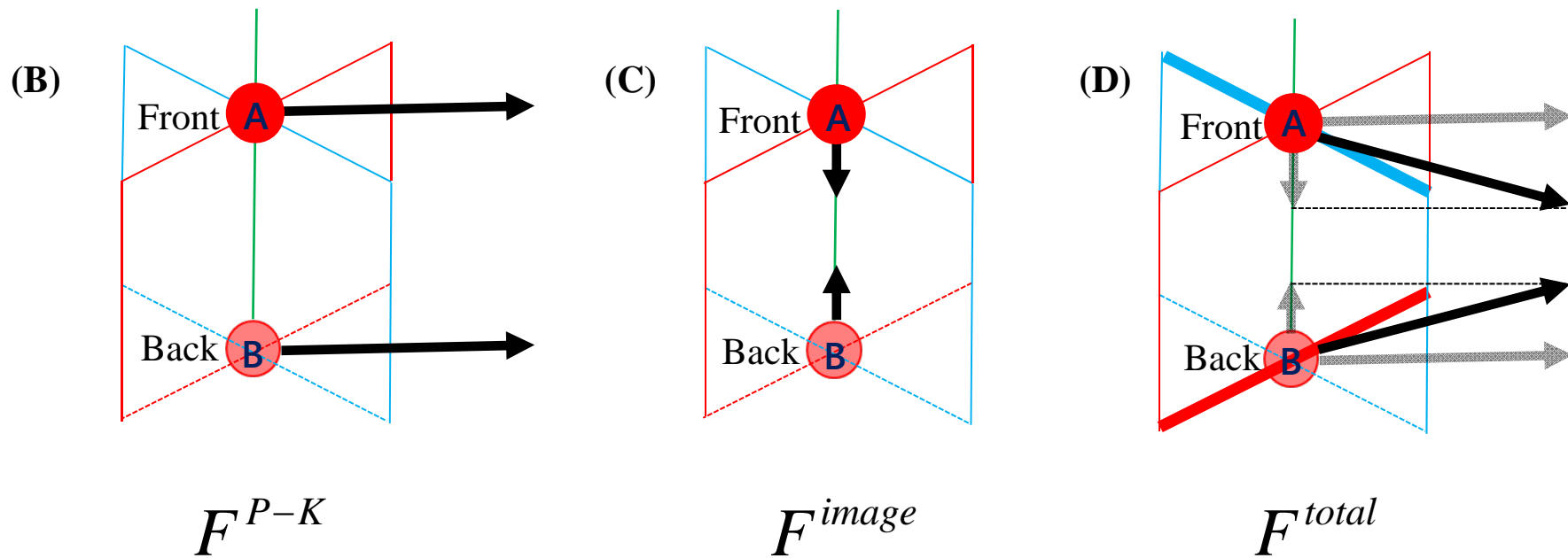


Figure 2

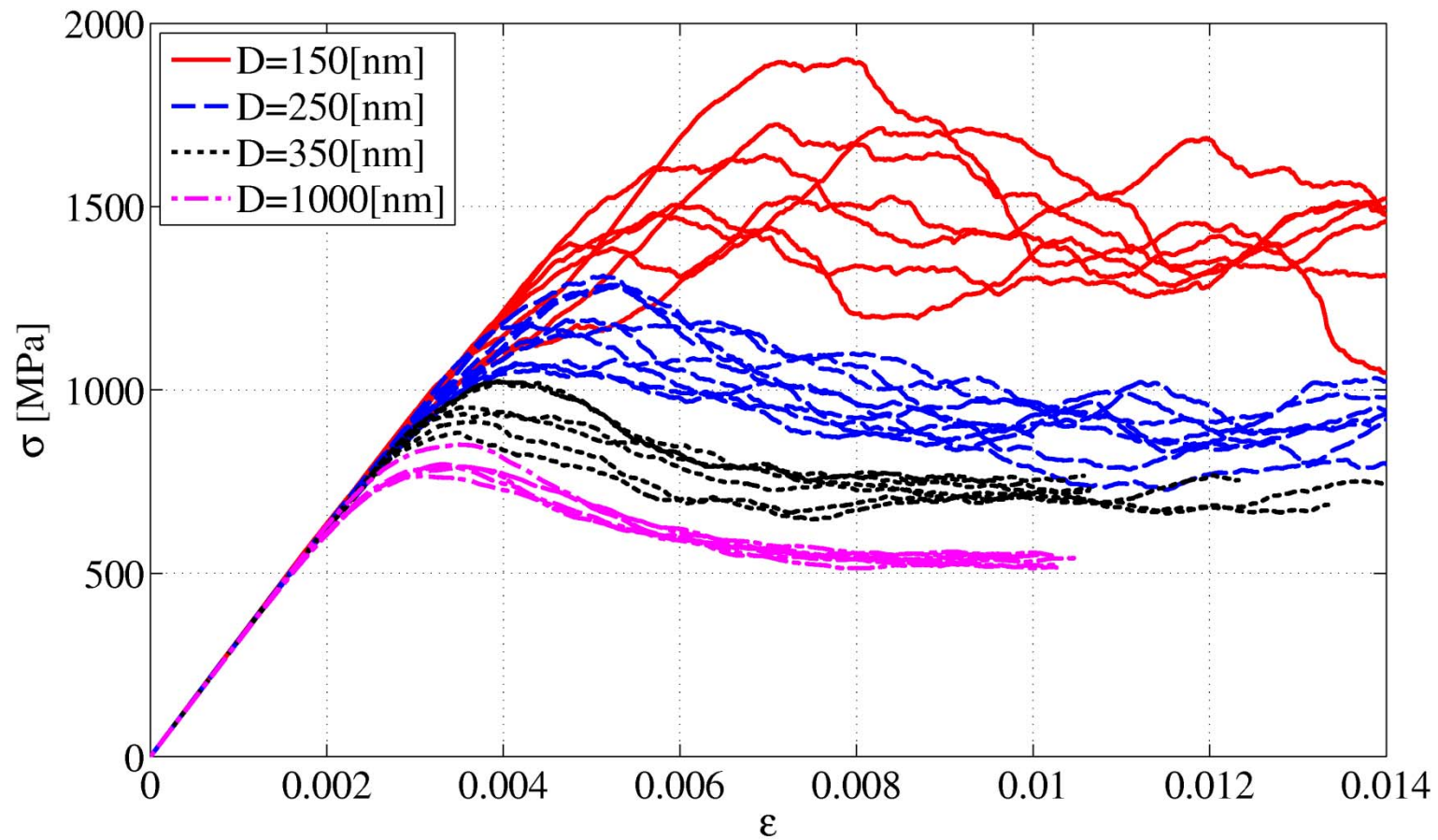


Figure 3A

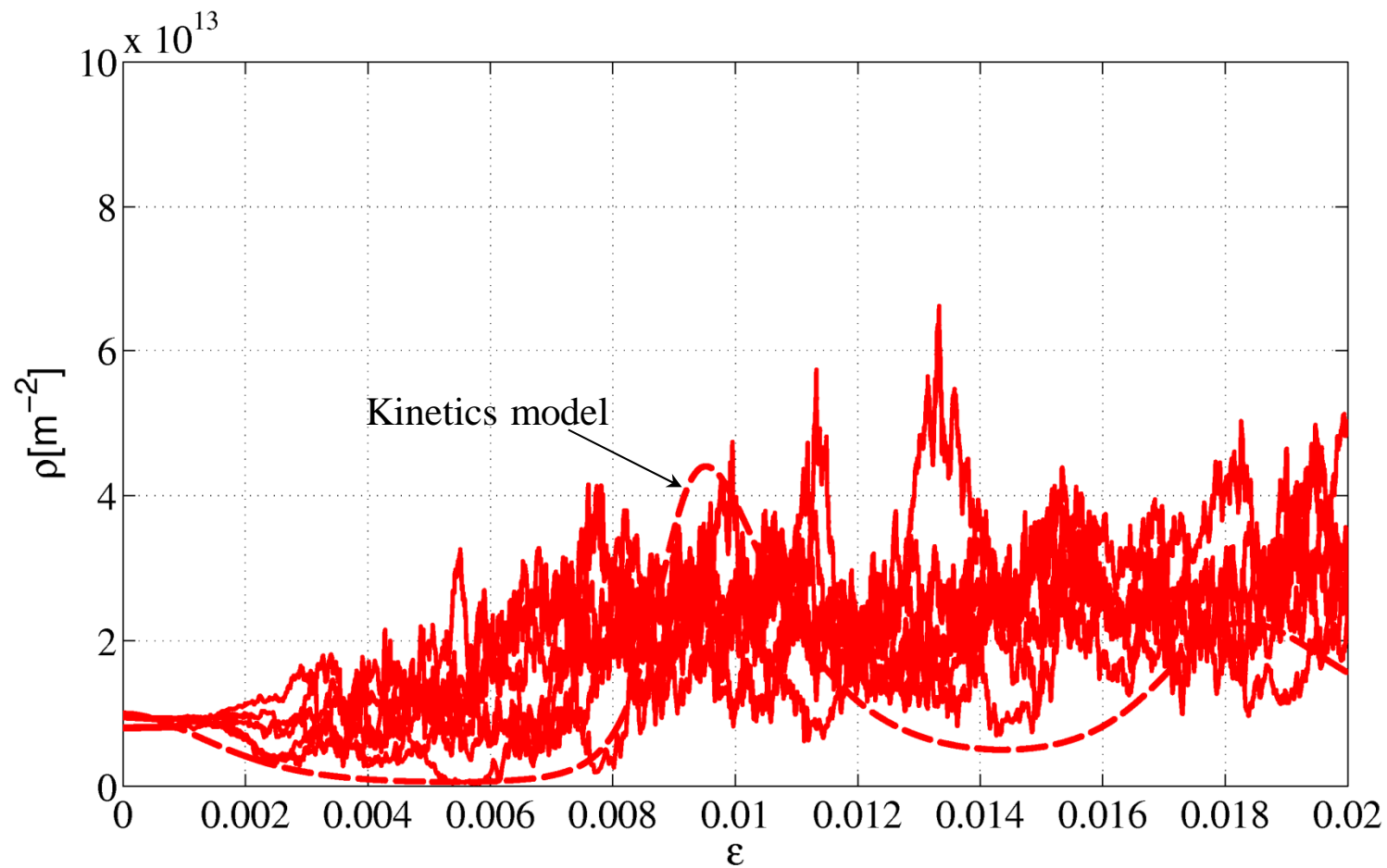


Figure 3B

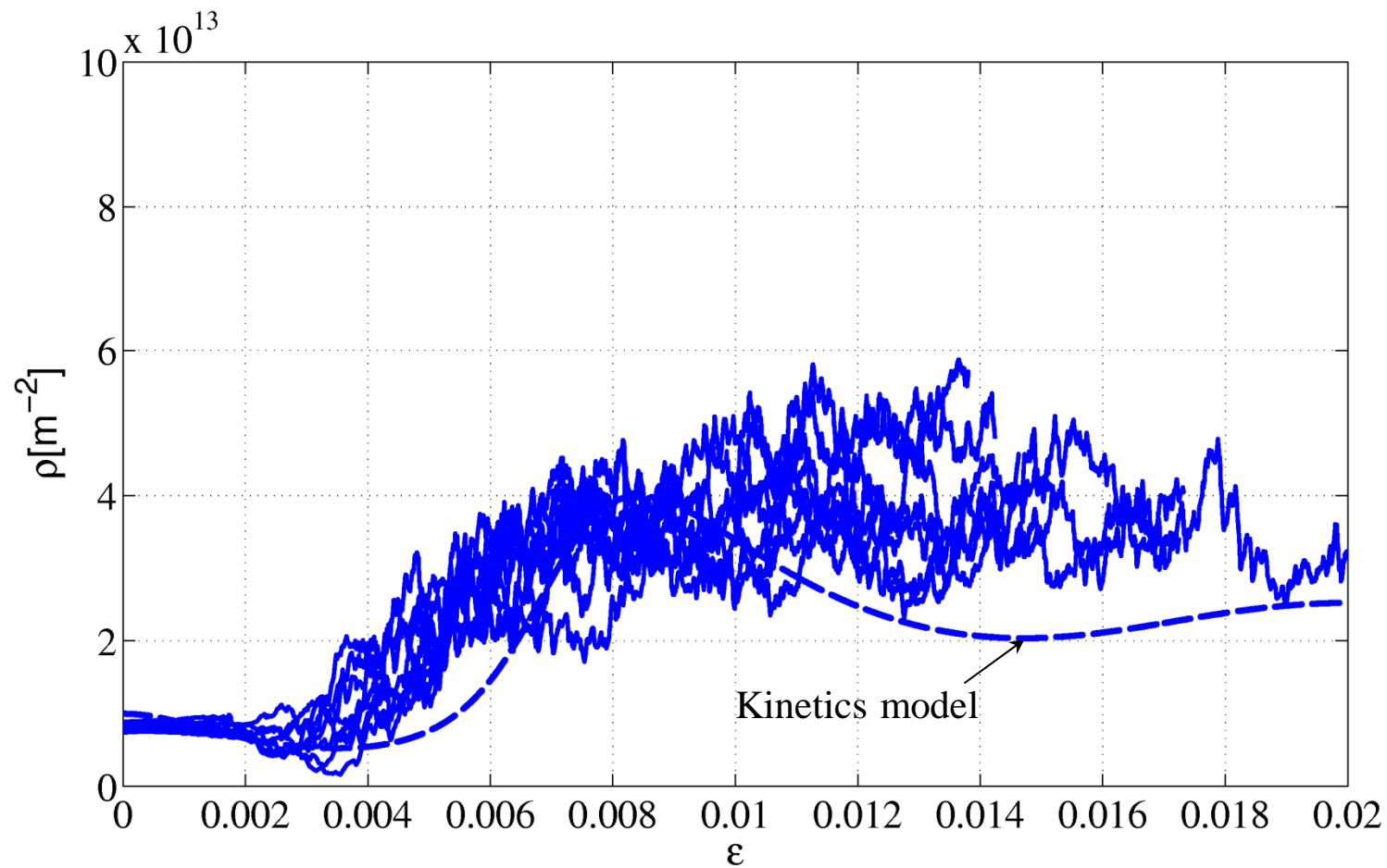


Figure 3C

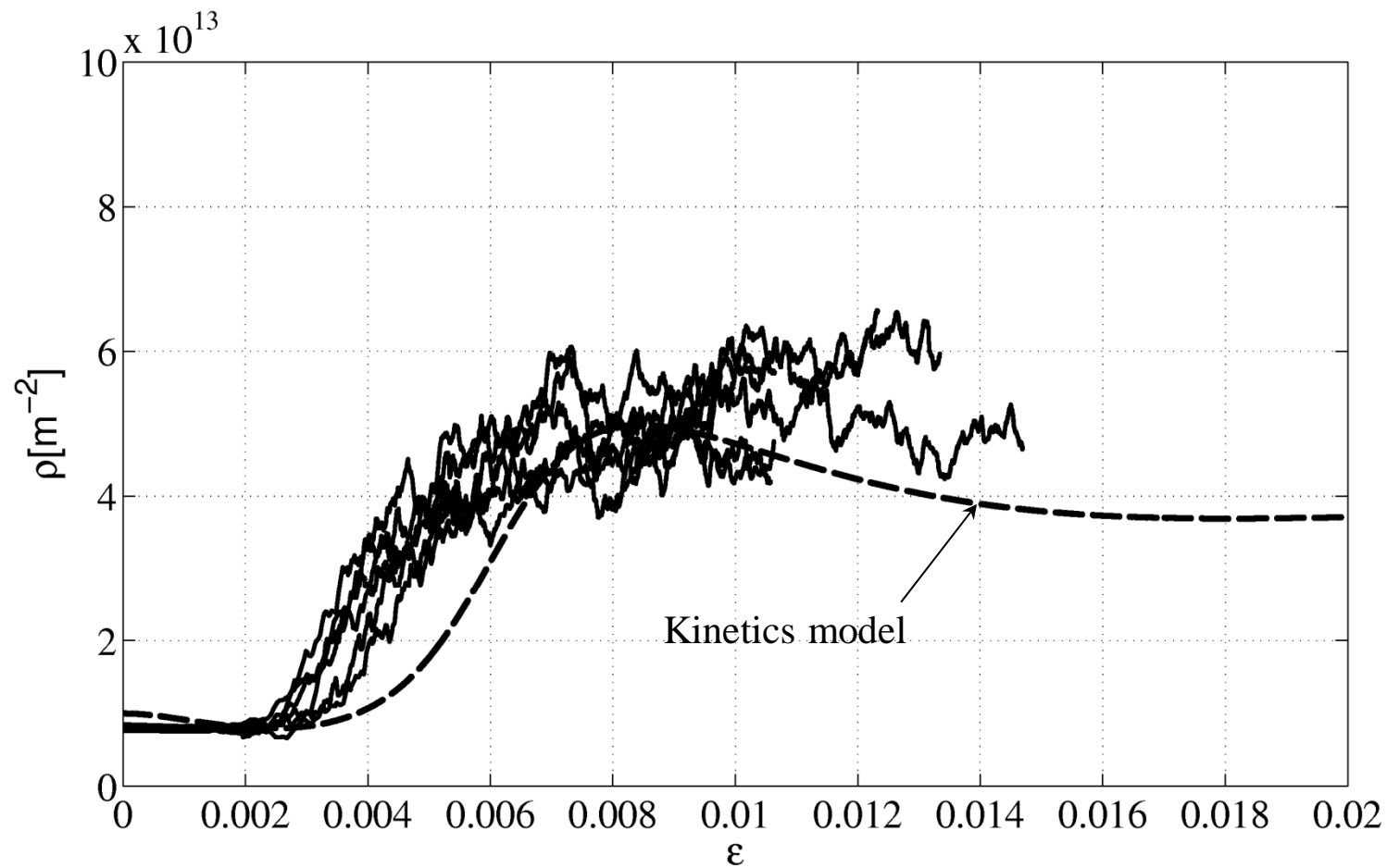


Figure 3D

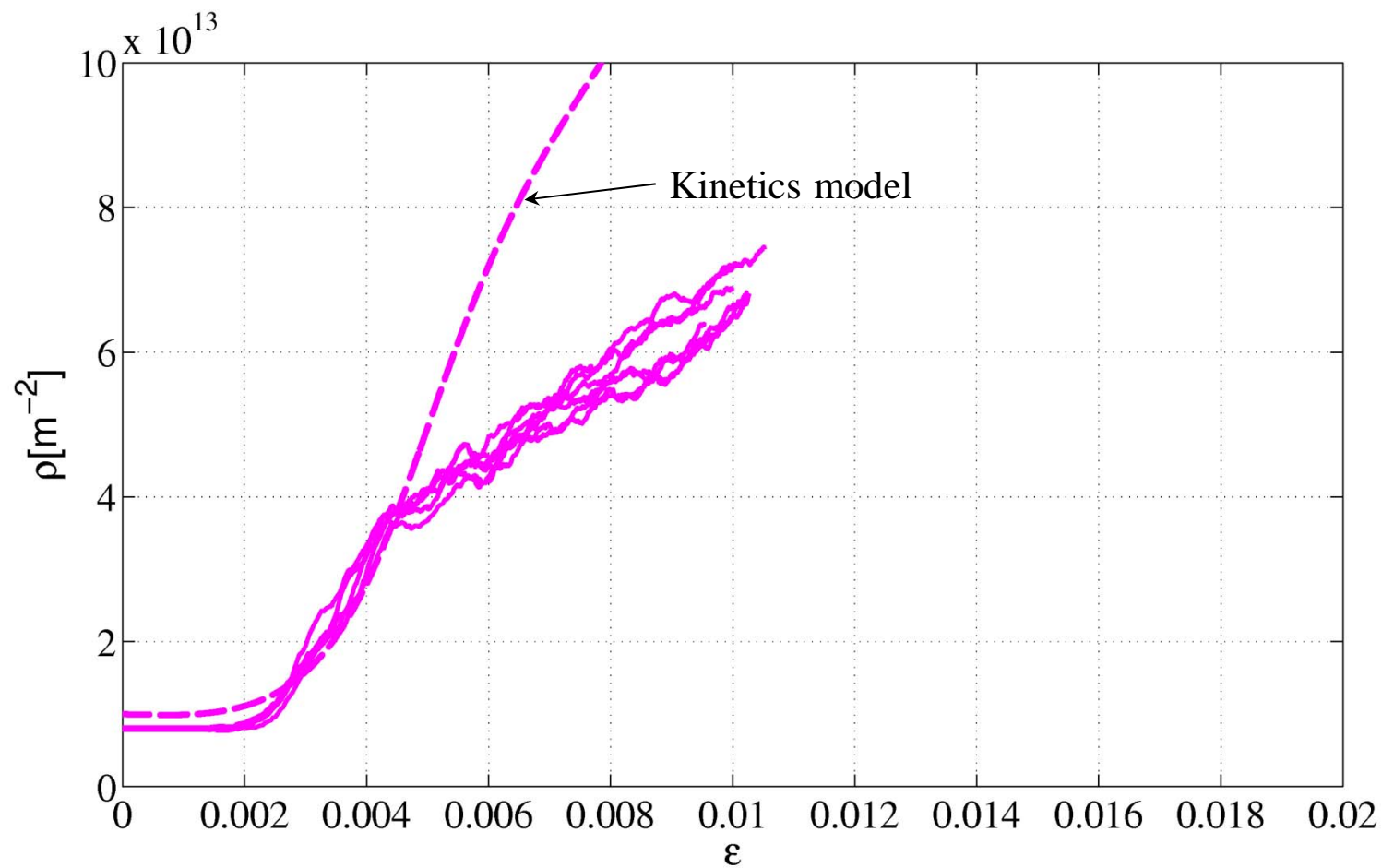
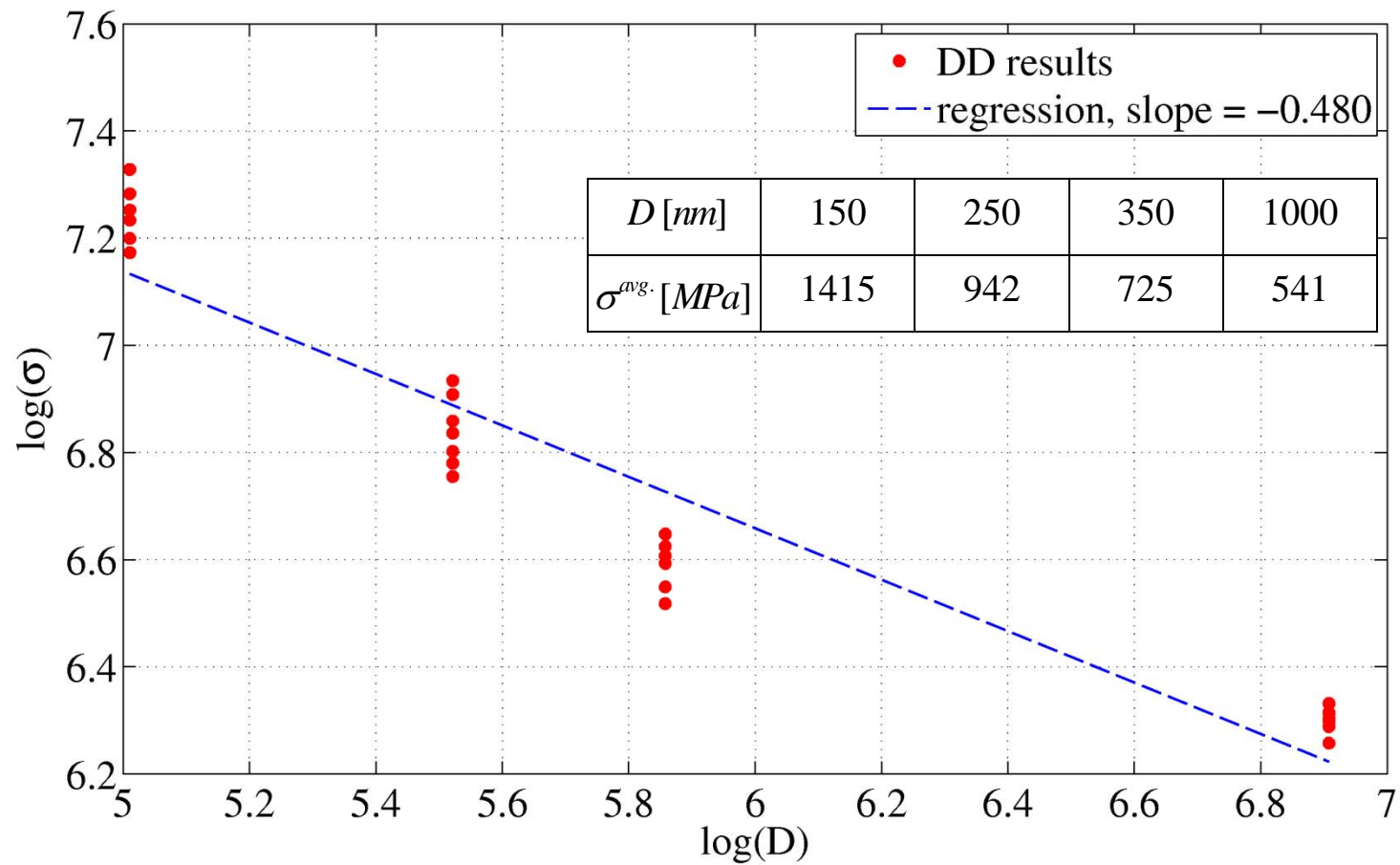


Figure 4



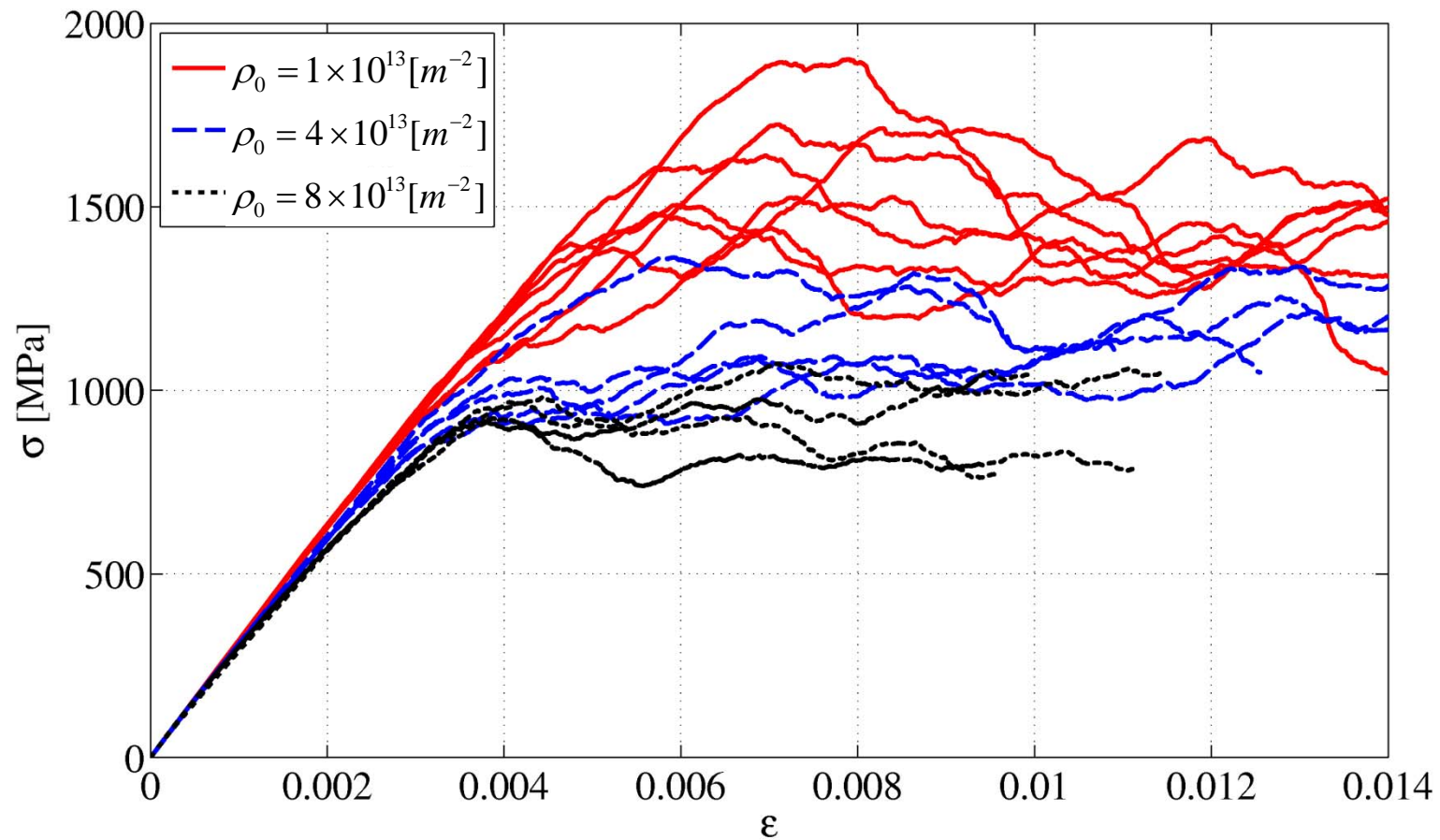


Figure 6

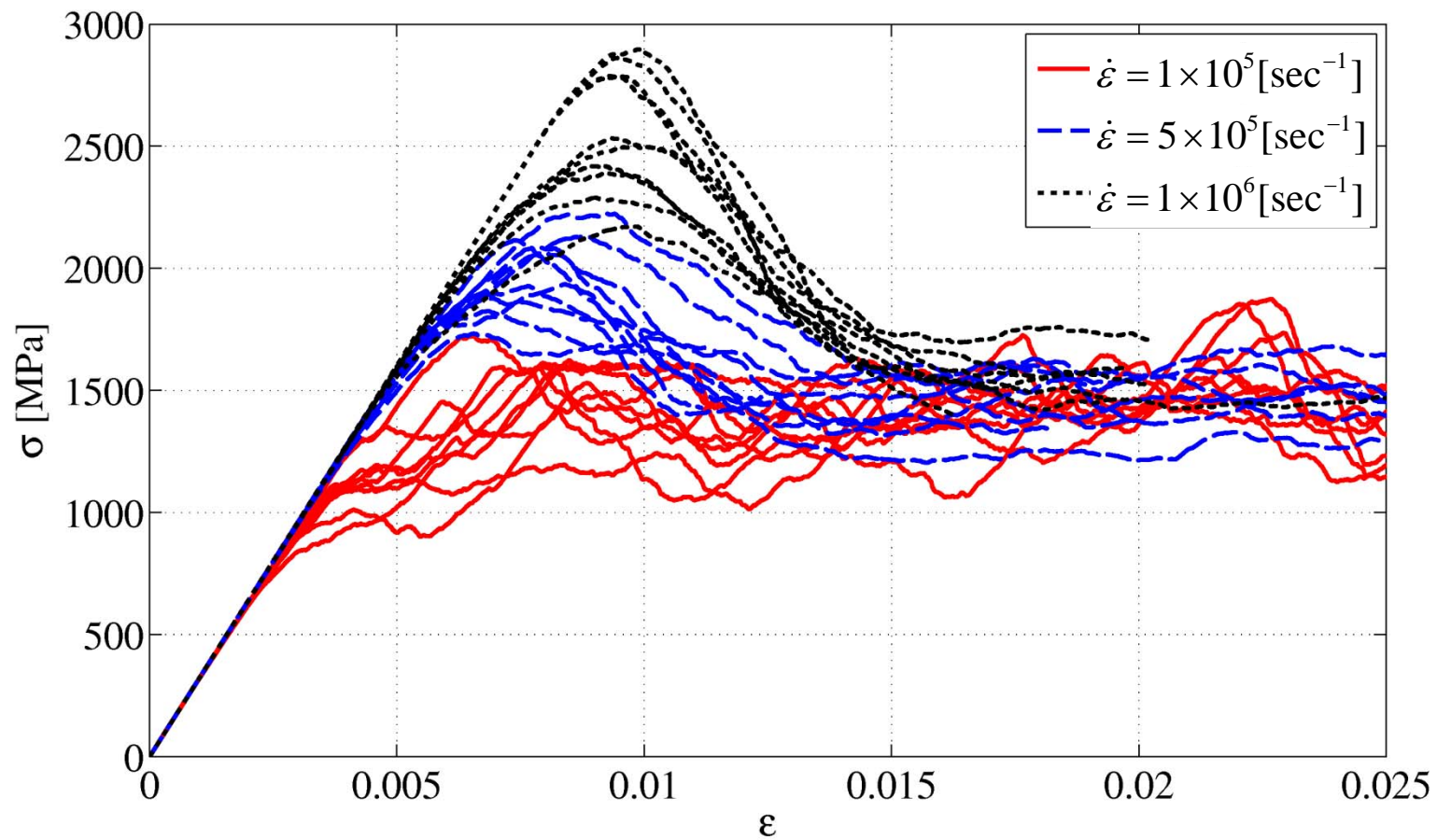


Figure 7

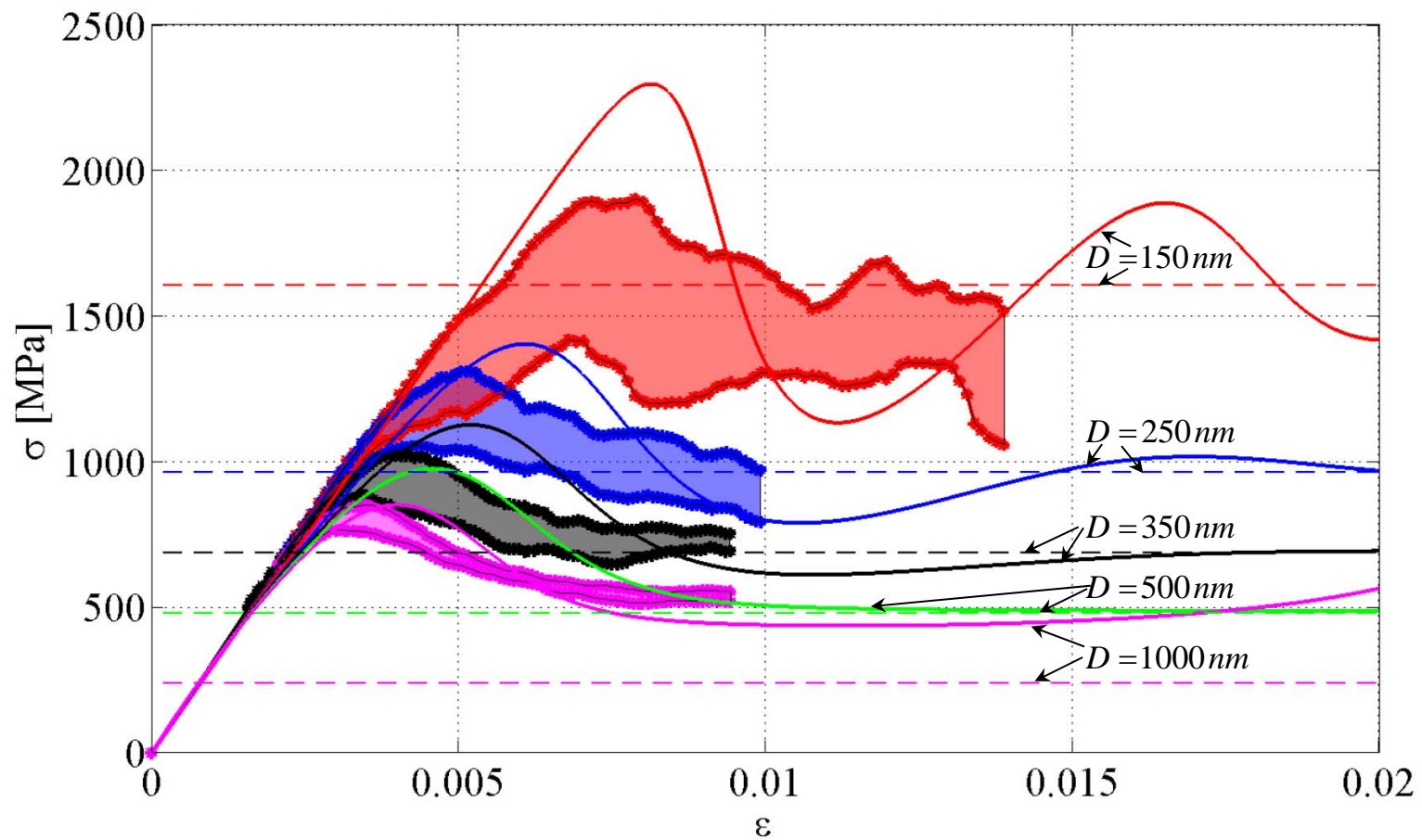


Figure 8A

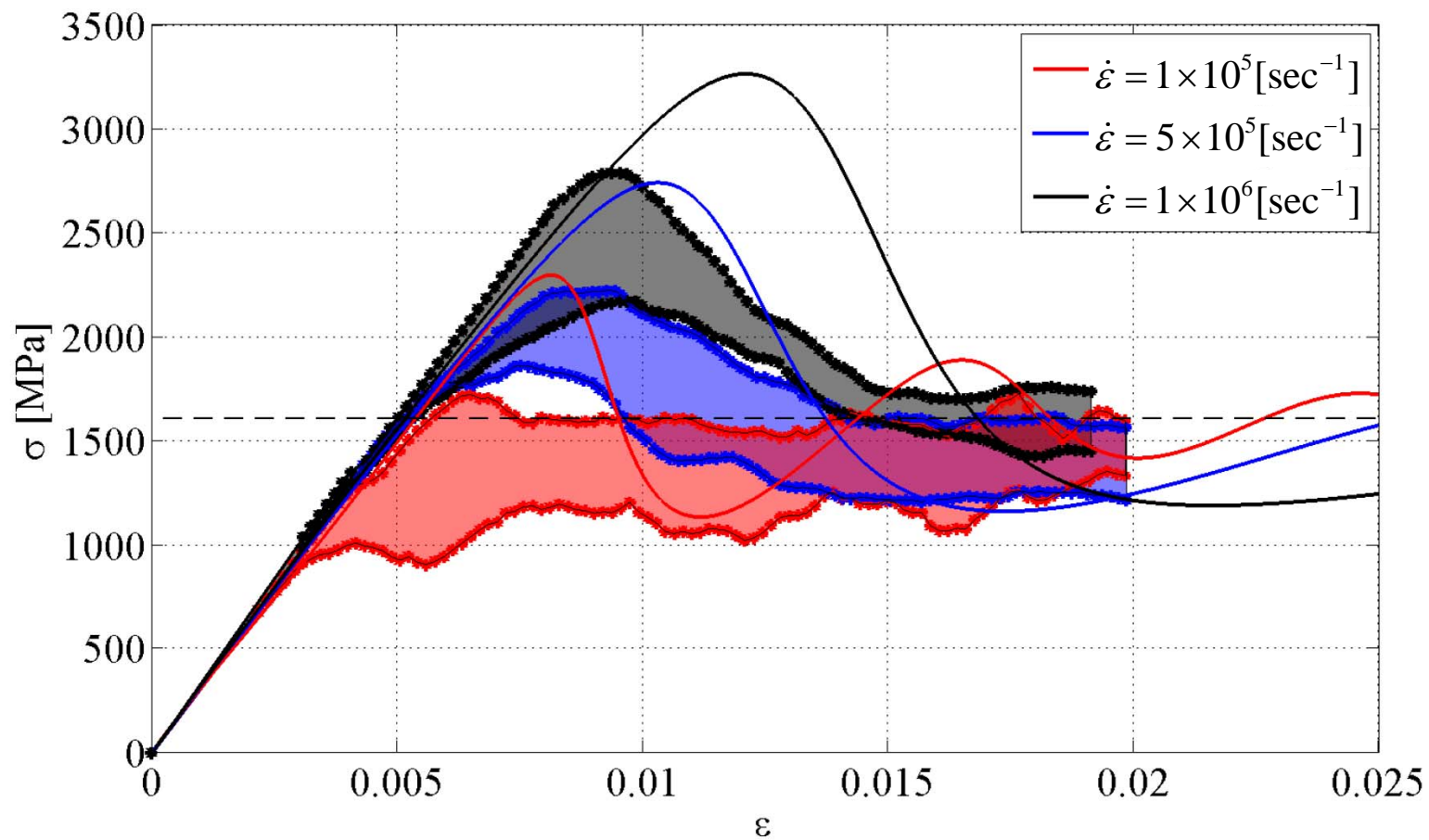


Figure 8B

